ROYAL SOCIETY OF CHEMISTRY

www.rsc.org/crystengcomm

Table of contents entry
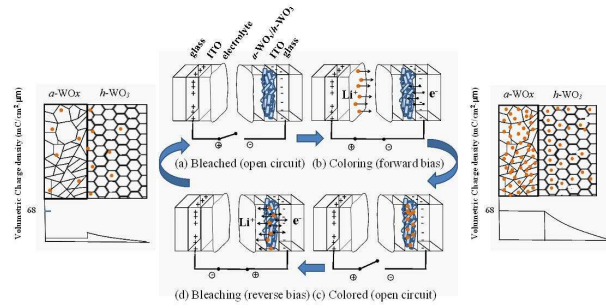
The h-WO$_3$/a-WO$_x$ core/shell heterostructures combine the assets of the constituent phases, and exhibit highly improved and balanced electrochromic properties.

Facile Synthesis of One-Dimensional Crystalline/Amorphous Tungsten Oxide Core/Shell Heterostructures with Balanced Electrochromic Properties

Yung-Chiun Her* and Chia-Chun Chang

5

One-dimensional (1D) crystalline/amorphous WO_3 core-shell heterostructures were synthesized
10 by a simple, two-step hydrothermal process. Single-crystalline hexagonal WO_3 (h-WO_3) nanorod
cores with diameters of about 200 nm and lengths of 6-7 μm were obtained in the first step.
Amorphous WO_x (a-WO_x) shells with thicknesses ranging from 8 to 40 nm were grown on the h-
WO_3 cores in the second step. The electrochromic properties of the devices based on the h-WO_3/a-
WO_x core-shell heterostructures were measured and compared with those based on the bare a-WO_x
15 and h-WO_3 nanorods. The optical modulation of coloration/bleaching at λ = 550 nm, is measured
to be 44% after coloration at -3.0 V for 180 s and bleaching at +2.0 V for 90 s. The coloration and
bleaching times are found to be 41 s and 6 s, respectively, and the coloration efficiency is 82
cm^2/C. After cyclic stability tests for 1000 cycles, the transmittance changes comparing with the
initial stage at the colored and bleached states are only 2.6 and 3.4 %, respectively. It appears that
20 the h-WO_3/a-WO_x core/shell heterostructures combine the assets of the constituent phases, and
exhibit highly improved and balanced electrochromic properties.

1. Introduction

Since the discovery of the electrochromic effect (EC) in
transition metal oxides in the mid-1960s,[1,2] tungsten oxide (WO_3)
25 has emerged as the most promising electrochromic material for
various electrochromic applications, such as energy-saving smart
windows, antiglare mirrors, and high contrast displays.[3]
Generally, electrochromism can be defined as the electrochemical
generation of color in accompaniment with an electron-transfer
30 reaction,[4] and electrochromic materials can be reversibly and
persistently switched between two optical states (coloration and
bleaching) by applying an external voltage. When a negative
electric field is applied, small cations such as H^+ and Li^+ in the
liquid or solid electrolyte can be intercalated into WO_3 film to
35 reduce WO_3 to M_xWO_3 (M = H^+, Li^+) with blue color. Under a
positive electric field, the reduced M_xWO_3 can be oxidized and
return to original transparent WO_3.[3] The electrochromic
performance of WO_3, in terms of optical modulation, coloration/
bleaching time, coloration efficiency, and cyclic stability,
40 strongly depends on its nature and structure. In the past decades,
most of the studies have been focusing on amorphous WO_3 (a-
WO_3) thin films due to their fast coloration/bleaching response
and high coloration efficiency.[5-7] However, a-WO_3 thin films also
suffer from poor electrochromic stability due to their poor
45 chemical and structural stabilities. In contrast, crystalline WO_3 (c-
WO_3) thin films are much more stable due to their denser
structure and slower dissolution rate in electrolytes, yet exhibit
the drawbacks of relatively lower charge density, poor coloration
efficiency, and slower switching response.[8-10] Therefore,
50 developing an electrochromic material with balanced

electrochromic properties has become a major target pursued by
researchers. Antonaia *et al.*[11] proposed an amorphous/crystalline
WO_3 double layer and reported that this double layer shows a
faster coloration response and a higher transmittance asymptotic
55 value for the bleaching phase than the amorphous or crystalline
single layer. The improvements of response time, coloration
efficiency, and electrochromic stability were also observed in
various nanocrystalline and nanoporous crystalline WO_3
films.[5,8,12,13] One-dimensional (1D) tungsten oxide
60 nanostructures, such as nanorods, nanowires, and nanotubes, are
expected to be able to further improve the performance of EC
devices by increasing the active surfaces in the electrochromic
process due to their large specific surface areas. Recently, 1D
WO_x nanostructures with various crystalline structures have been
65 synthesized using physical and chemical approaches, and the
integrated electrochromic properties of the assembled WO_x
nanostructure films were also reported.[10,14-16] Liao *et al.*[14]
synthesized monoclinic $W_{18}O_{49}$ nanowires by a thermal
evaporation process and prepared an EC device adopting the
70 $W_{18}O_{49}$ nanowires as the electrochromic layer. The as-fabricated
EC device demonstrated a maximum optical contrast of 34.5% at
λ = 700 nm, and could be cycled up to 1000 cycles. Gu *et al.*[15]
prepared hexagonal WO_3 (h-WO_3) nanowires by a simple
hydrothermal method without any templates and catalysts. The
75 as-prepared h-WO_3 nanowires when used as the anodic material
of a Li-ion battery delivered charge and discharge capacities of
165 and 218 mAhg^{-1}, respectively, implying large promotion of
reaction reversibility of Li intercalation/extraction in h-WO_3
nanowires. Wang *et al.*[10] and Szilágyi *et al.*[16] also synthesized
80 uniform crystalline WO_3 nanorods using a hydrothermal process,
and demonstrated that the as-synthesized crystalline WO_3

nanorods exhibit high electrochromic stability and comparable color display, contrast, and coloration/bleaching response.

Although 1D crystalline WO₃ nanostructures demonstrated improvement in the electrochromic stability, further improvements in response time and coloration efficiency of EC devices are still a big challenge. Park *et al.*[17] developed a sub-5 nm thick tungsten oxide nanorod-based electrochromic system by a colloidal approach and achieved highly improved response time and color efficiency. It is believed that well-defined nm-thick crystalline metal oxide materials, with lots of amorphous surface areas should be good candidates for further improving the performance of EC devices. Accordingly, 1D nanoscale heterostructures comprised of amorphous and crystalline WO₃ could be expected to demonstrate better electrochromic performance than reported 1D crystalline WO₃ nanostructures. In this work, we synthesized 1D crystalline/amorphous WO₃ core-shell heterostructures using a simple, two-step hydrothermal method. EC devices based on the as-grown 1D crystalline/amorphous WO₃ core-shell heterostructures were fabricated, and their electrochromic properties were measured and compared with those obtained from devices based on bare crystalline or amorphous WO₃ nanorods. We also discussed the possible reasons behind the highly improved and balanced electrochromic properties of our 1D crystalline/amorphous WO₃ core/shell heterostructures.

2. Experimental

1D crystalline/amorphous WO₃ core-shell heterostructures were synthesized using a simple, two-step hydrothermal process. For the crystalline WO₃ core nanostructures, an aqueous solution was prepared by dissolving 0.2 g of Na₂WO₄ and 0.1 g of Na₂SO₄ in 7 ml of deionized water, and then 1M HCl was slowly dropped into the solution with stirring until the pH value of the solution reached 2.0. The precursor solution, contained in a Teflon-lined stainless steel autoclave, was kept at a constant temperature of 180 °C for 24h without stirring or shaking. Afterwards, the autoclave was cooled to room temperature, and the resultant products were subsequently washed with deionized water and dried naturally in the air. For the thin amorphous WO$_x$ shells, the preparation of the precursor solution was similar to that for single-crystalline WO₃ core nanostructures, except that 1.0 g of Na₂WO₄ and 0.8 g of Na₂SO₄ were dissolved in 20 ml of deionized water. The precursor solution, mixed with 0.01 g of previously synthesized crystalline WO₃ core nanostructures, was introduced in a closed Pyrex bottle with an autoclavable screw cap. The bottle was then bathed in 90 °C water, heated and stirred by a heating magnetic stirrer for 6 h. The resultant products were washed with deionized water and dried naturally in the air. For the purpose of comparison, amorphous WO$_x$ nanorods were also prepared by a similar hydrothermal process. The precursor solution, contained in a Teflon-lined stainless steel autoclave was the same as that for amorphous WO$_x$ shells. The autoclave was heated to 110 °C for 24h. Typical FESEM and TEM bright-field images of the as-grown amorphous WO$_x$ nanorods are shown in figures S1(a) and (b). The highly dispersed selected area electron diffraction (SAED) patterns confirm that the as-grown nanorods are of a completely amorphous state. For the fabrication of EC

devices, bare amorphous and crystalline WO₃ nanorods, as well as crystalline/amorphous WO₃ core-shell heterostructures were dispersed in methanol, respectively, to form a suspension with a WO₃ concentration of 0.03 g/l. Then 0.5 ml of suspension was dropped onto a clean ITO glass with a bare area of 1 cm × 1 cm bonded by Scotch tapes, and dried at room temperature to form a transparent film. A mixture of 1 M LiClO₄ with 1% UV resin was then dropped onto the WO₃ transparent film on the ITO glass, to act as a pure ion conductor (i.e. electrolyte). The half-cell was covered by another ITO glass and UV cured for 12h to harden the polymer electrolyte. Epoxy resin was used to seal the edge of the EC device to provide more mechanical strength, and reduce the absorption of moisture from the atmosphere. The morphologies and crystalline structures of the as-synthesized products were examined and characterized using field-emission scanning electron microscope (FESEM, JSM-6700), X-ray powder diffractometer (PANalytical X'Pert PRO) using Cu K$_\alpha$ (λ = 0.15405 nm) radiation, and high-resolution transmission electron microscope (HRTEM, JEM-2100) using an acceleration voltage of 200 kV. The electrochemical measurements were carried out by a three-electrode system using 1M LiClO₄ with 1% UV resin as the supporting electrolyte, platinum (Pt) wire as the counter electrode and saturated calomel electrode (SCE) as the reference electrode. In situ coloration/bleaching switching characteristics of the as-fabricated EC devices were recorded by monitoring the variation in transmittance at a wavelength of 550 nm using a SHIMADZU UV-VIS spectrophotometer (UV-1601PC). The coloration and bleaching potentials were kept constant at -3.0 V and +1.5 V, respectively, using a programmable potentiostat. It should be noted that the transmittance measurements were conducted by inserting the EC devices into the standard sample compartment and no reference sample was inserted into the reference side.

3. Results and Discussion

Fig. 1(a) shows a typical FESEM image of the as-synthesized products prepared in the first step. Large-scale and uniform rod-like nanostructures (nanorods) with diameters of 150-200 nm and lengths of 6-7 μm were obtained. As we closely examined the morphologies of the as-synthesized nanorods (shown in the inset of Fig. 1(a)), it can be seen that these nanorods have flat tip ends and are enclosed by numerous nanostrips. The representative XRD diffraction patterns of the nanorods are shown in Fig. 1(b). All of the diffraction peaks can be readily indexed to the hexagonal WO₃ (*h*-WO₃) phase with lattice constants of *a* = 7.32 Å and *c* = 7.67 Å, which agrees well with the reported value (*a* = 7.324 Å, *c* = 7.668 Å) from the JCPDS card (No. 85-2460). No other tungsten oxide phases and tungsten oxide hydrates (WO₃·xH₂O) were detected, indicating that pure *h*-WO₃ nanorods were obtained in the first step. Fig. 1(c) shows a representative TEM bright-field image and the SAED patterns of a single *h*-WO₃ nanorod. It is clear that the as-synthesized *h*-WO₃ nanorod has a fairly uniform diameter along almost its entire length. The SAED patterns can also be perfectly indexed to *h*-WO₃, and the growth direction of the nanorod is determined to be along the [0001] direction (*c*-axis). Regular diffraction spots support that the as-synthesized *h*-WO₃ nanorods are single crystalline. It is known that WO₃ can crystallize into several crystalline structures.
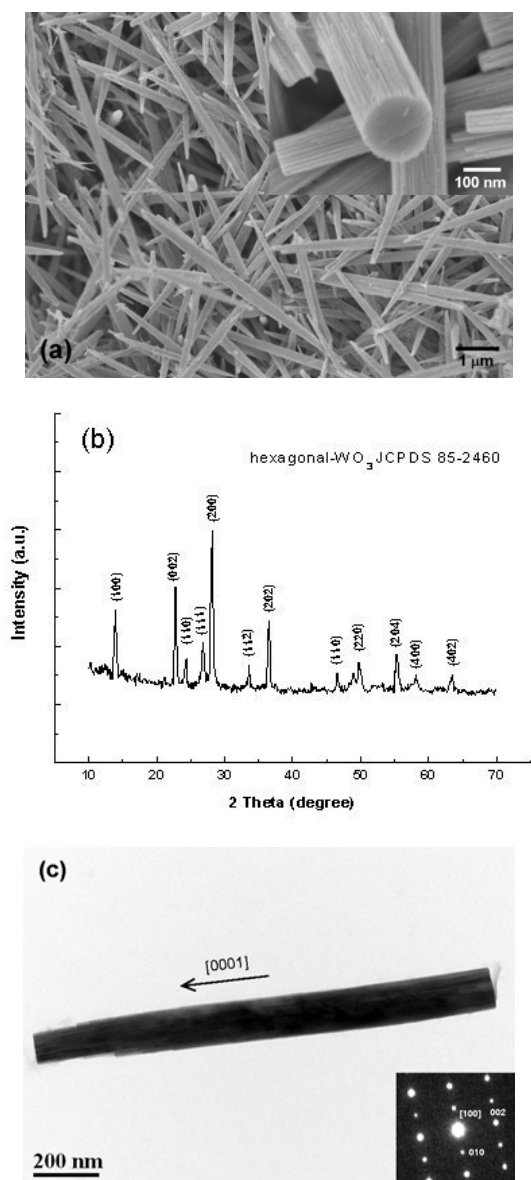
Fig. 1 (a) FESEM image and (b) XRD patterns of the as-synthesized products prepared in the first step, and (c) TEM bright-field image and SAED patterns of a single nanorod.

Among them, hexagonal WO_3 is of particular interest for electrochromic applications, because its tunnel structure makes it act as an ideal intercalation host for obtaining hexagonal tungsten bronzes M_xWO_3.[15] Normally h-WO_3 is a metastable phase, and will transform into monoclinic WO_3 phase at higher temperatures. The formation of the hexagonal WO_3 nanorods in this work can be attributed to the presence of Na^+ ions, which stabilize the hexagonal structure by locating in the hexagonal channels to block the thermodynamically favored hexagonal-to-monoclinic transformation.[16] It is also believed that the capping action of Na^+ ions is responsible for the preferential growth of h-WO_3 nanorods along the c-axis.[16]

After the synthesis of crystalline h-WO_3 nanorod cores, amorphous WO_x shells were subsequently grown onto the cores
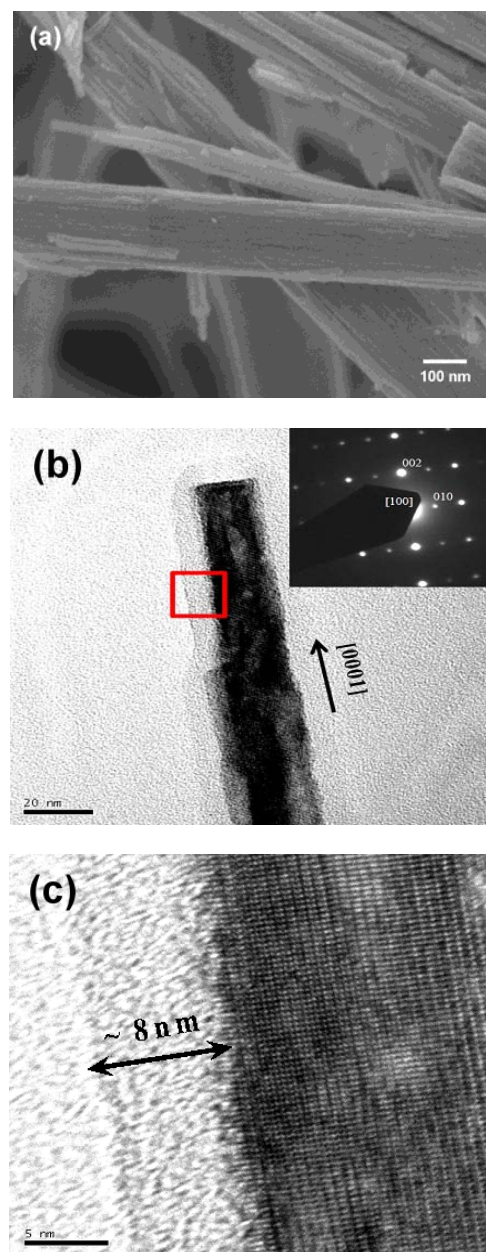
Fig. 2 (a) FE-SEM image of the as-grown crystalline/amorphous WO_3 core/shell nanorods, (b) TEM and (c) HRTEM images of one crystalline/amorphous WO_3 core/shell nanorod.

by another hydrothermal process in the second step. Fig. 2(a) shows a typical FESEM image of the resultant h-WO_3/a-WO_x core/shell nanostructures. It can be seen that the morphologies of the nanostructures remained a rod-like shape, indicating that conformal a-WO_x shells have been grown on the surfaces of the h-WO_3 nanorods. Figs. 2(b) and 2(c) show the representative TEM and HRTEM images of a single h-WO_3/a-WO_x core/shell nanorod, respectively. Clearly, a thin layer of a-WO_x shell with a thickness of about 8 nm, has been uniformly grown on the single-crystalline h-WO_3 cored nanorod to form the crystalline/amorphous WO_3 core/shell heterostructure. The lattice spacing of 0.39 nm of adjacent lattice planes in the h-WO_3 cored nanorod,

corresponds to the *d*-spacing of (0001) planes. This confirms again that the *h*-WO$_3$ nanorods grow along the *c*-axis. It should be noted that the thickness of the *a*-WO$_x$ shell can be controlled by the synthesis time in the second step. As the synthesis time was increased to 12 and 24 h, the average thickness of the *a*-WO$_x$ shell increased to ~15 and 40 nm, respectively.

As mentioned earlier, the performance of an EC device is usually evaluated by the metrics of optical modulation, coloration /bleaching response time, coloration efficiency, as well as cyclic stability. Fig. 3 shows the in situ coloration/ bleaching switching responses of the EC devices based on the *a*-WO$_x$ and crystalline *h*-WO$_3$ nanorods, and *h*-WO$_3$/*a*-WO$_x$ core/shell heterostructures. by applying a coloration voltage of –3.0 V for 180 s and a bleaching voltage of +1.5 V for 90 s. It can be seen that the transmittance at λ = 550 nm for *a*-WO$_x$ and crystalline *h*-WO$_3$ nanorods, and *h*-WO$_3$/*a*-WO$_x$ core/shell heterostructures dropped from 77, 80, and 78 % to 26, 45, and 32 %, respectively, after applying a coloration voltage of –3.0 V. The transmittance then returned to 71, 71, and 76 %, respectively, after applying a bleaching voltage of +1.5 V. The *a*-WO$_x$ nanorods could reach the deepest coloration level, while the *h*-WO$_3$/*a*-WO$_x$ core/shell heterostructures exhibited the highest transmittance asymptotic value for the bleaching phase. Moreover, the EC devices based on *a*-WO$_x$ nanorods and *h*-WO$_3$/*a*-WO$_x$ core/shell heterostructures exhibited similar optical modulations of 45 and 44 %, respectively, which are much higher than that of 25% for the device based on the crystalline *h*-WO$_3$ nanorods. Here, the coloration and bleaching times were defined as the time required for 70% changes in optical modulation. For coloration, the response time for *h*-WO$_3$/*a*-WO$_x$ core/shell heterostructures (41 s) is slightly longer than that for *a*-WO$_x$ nanorods (39 s), but much shorter than crystalline *h*-WO$_3$ nanorods (65 s). For bleaching, all of the devices demonstrated a fast response time of only 6 s. The coloring response times were much longer than bleaching response times, because the conductivity of bleached-state WO$_3$ is slower than that of colored-state LiWO$_3$.[18] The optical modulation and coloration and bleaching response times of *h*-WO$_3$/*a*-WO$_x$ core/shell heterostructures are similar to those of *a*-WO$_x$ nanorods, but are much superior to those of crystalline *h*-WO$_3$ nanorods.

It is well-known that the coloration/bleaching switching of WO$_3$ in Li$^+$ electrolytes, is due to the intercalation/deintercalation of electrons and charge-balancing Li$^+$ ions. In order to explore the Li$^+$ ion storage capacities of *a*-WO$_x$ nanorods, crystalline *h*-WO$_3$ nanorods, and *h*-WO$_3$/*a*-WO$_x$ core/shell heterostructures, chronoamperometry measurements were carried out, and the current density responses with time were recorded when a cycling pulse potential was applied between –3.0 V and +1.5 V, as shown in Fig. 4(a). The integration of current density with time extracted from coloration parts, representing cathodic charge density or ion storage capacity, is indicative of the amount of Li$^+$ ions incorporated into the electrochromic layer during coloration. The cathodic charge density for maximum contrast for *h*-WO$_3$/*a*-WO$_x$ core/shell heterostructures was calculated to be about 8.0 mC cm^{-2}, which is slightly higher than that for crystalline *h*-WO$_3$ nanorods (7.7 mC cm^{-2}), but is much lower than that for *a*-WO$_x$ nanorods (9.5 mC cm^{-2}). For practical EC applications, lower charge insertion and extraction usually implies that a long-term
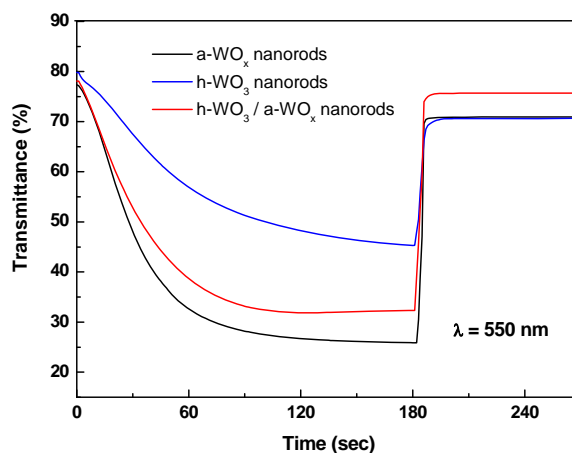
Fig. 3 In situ coloration/bleaching switching responses of the EC devices based on *a*-WO$_x$ and *h*-WO$_3$ nanorods and *h*-WO$_3$/*a*-WO$_x$ core/shell heterostructures by applying a coloration voltage of -3.0 V for 180 s and a bleaching voltage of +1.5 V for 90 s.
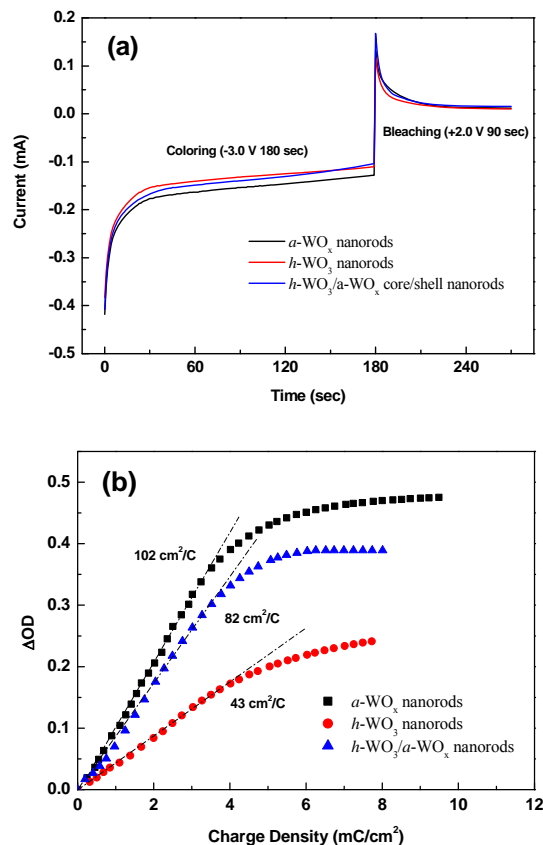
Fig. 4 (a) Chronoamperometry measurement for voltage steps between -3.0 V and +1.5 V, and (b) variation of in situ OD with charge density for the EC devices based on *a*-WO$_x$ and *h*-WO$_3$ nanorods and *h*-WO$_3$/*a*-WO$_x$ core/shell heterostructures.

cyclability can be achieved in a real device during operation.[19] Accordingly, we expect that EC device based on h-WO$_3$/a-WO$_x$ core/shell heterostructures, to exhibit long-term cyclability that are comparable to device based on crystalline h-WO$_3$ nanorods,

5 but are superior to device based on a-WO$_x$ nanorods.

Another important parameter to characterize the performance of an electrochromic material, is its coloration efficiency (CE), which can be expressed as:

10   CE = ΔOD/Q = log(T$_b$/T$_c$)/Q   [1]

where ΔOD is the change in optical density (OD), Q is the charge density (mC cm^{-2}), and T$_b$ and T$_c$ are the transmittance in bleached and colored states, respectively. High CE means that

15 large optical modulation can be readily achieved by small charge insertion or extraction. Fig. 4(b) shows the plot of ΔOD versus charge density, where OD was measured at a wavelength of 550 nm. From the slopes of the lines fitting to the curves, the CE values of the devices made from a-WO$_x$ nanorods, h-WO$_3$/a-WO$_x$

20 core/shell heterostructures, and crystalline h-WO$_3$ nanorods were determined to be 102, 82, and 43 cm^2/C, respectively. It indicates that the h-WO$_3$/a-WO$_x$ core/shell heterostructures can preserve a relatively high CE, which is about 80% of the a-WO$_x$ nanorods, and almost twice that of the crystalline h-WO$_3$ nanorods. It

25 should be noted that the EC values for our a-WO$_x$ nanorods and h-WO$_3$/a-WO$_x$ core/shell heterostructures are easily comparable with the state-of-the-art of about 84 cm^2/C, for nanostructured WO$_3$ films transformed from sol-gel derived amorphous WO$_3$ films reported by Deepa et $al.$[5]

30   Based on the experimental results, it can be confirmed that h-WO$_3$/a-WO$_x$ core/shell heterostructures inherit all the advantageous electrochromic properties from a-WO$_x$, such as a large optical modulation, short coloration and bleaching response times, and high coloration efficiency. However, a-

35 WO$_x$ films synthesized from wet-chemical methods usually suffer from poor long-term durability due to their poor chemical and structural stabilities. To evaluate the capability of our h-WO$_3$/a-WO$_x$ core/shell heterostructures for use in practical EC device, a series of cyclic stability tests were

40 conducted. Fig. 5 shows the transmittance variations as a function of coloration-bleaching cycle for EC devices based on a-WO$_x$ and h-WO$_3$ nanorods, and h-WO$_3$/a-WO$_x$ core/shell heterostructures. It can be seen that for all three types of EC devices, the transmittance at the bleached state showed abrupt

45 drops after 10 cycles, and then decreased gradually, while the transmittance at colored state increased gradually. After 1000 cycles, the transmittance deviations for the h-WO$_3$/a-WO$_x$ core/shell heterostructures at bleached and colored states, compared with values measured after 10 cycles, were found to

50 be 2.6 and 3.4%, respectively. This resulted in a 6.0% degradation of the optical modulation. Meanwhile, the transmittance deviations at bleached and colored states, and degradation of optical modulation were found to be 6.8, 6.3, and 13.1%, respectively, for a-WO$_x$ nanorods, and 3.5, 1.4,

55 and 4.9%, respectively, for h-WO$_3$ nanorods. It is evident that h-WO$_3$/a-WO$_x$ core/shell heterostructures also show comparable electrochromic stability with crystalline h-WO$_3$
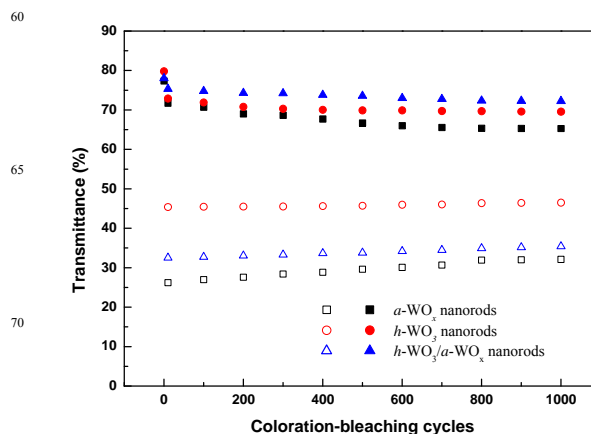
Fig. 5 Transmittance variations as a function of coloration-bleaching cycle for the EC devices based on a-WO$_x$ and h-WO$_3$ nanorods and h-WO$_3$/a-WO$_x$ core/shell heterostructures.

80 nanorods, which agrees with the previous prediction based on cathodic charge density for maximum contrast.

Table 1 summaries the optical modulations, cathodic charge densities, coloration and bleaching times, coloration efficiencies, and degradation of optical modulation after 1000 cycles for EC

85 devices based on a-WO$_x$ and h-WO$_3$ nanorods and h-WO$_3$/a-WO$_x$ core/shell heterostructures. Without a doubt, h-WO$_3$/a-WO$_x$ core/shell heterostructures combine assets of the constituent phases, which are large optical modulation, fast coloration/ bleaching responses, and high coloration efficiency from a-WO$_x$

90 and good cyclic stability from crystalline h-WO$_3$.

It has been reported that the electrochromic coloration of tungsten oxide upon H$^+$ or Li$^+$ ion insertion is influenced by crystallinity, microstructure, and oxygen deficiency of the film.[20,21] For the amorphous case, the coloration mechanism

95 resulting from injection of positive ions and electrons is usually attributed to small polaron absorption proposed by Schirmer et $al.$[22] The inserted electrons are localized in the W^{5+} sites and polarize their surroundings to induce lattice vibrations.[23,24] The inserted ions (M$^+$) either lie in the centers of perovskite units, or

100 are chemically bonded with the interstitial oxygen atoms. Consequently, they are spatially separated from the electrons and this spatial separation creates a polaron.[25] The incident photons are absorbed by these small polarons that can hop from one site to another between two adjacent sites of

105 tungsten W^{5+} and W^{6+}, where transfer of electrons between sites denoted as i and j can be schematically written as W$_i^{5+}$ + W$_j^{6+}$ + photon → W$_i^{6+}$ + W$_j^{5+}$.[3] For the crystalline case, there is no spatial separation between inserted ions and electrons, and the coloration mechanism is attributed to a Drude-mode-

110 like free electron absorption with a behavior very similar to a heavily doped semiconductor with ionized impurities.[3,23] As cations and electrons are inserted into crystalline tungsten oxide films, the electrons enter extended states in the WO$_3$ band structure and experience scattering by impurities and/or

115 phonons, rather than enter localized states as in amorphous

Table 1. Summary of the electrochromic properties for the EC devices based on a-WO$_x$ and h-WO$_3$ nanorods and h-WO$_3$/a-WO$_x$ core/shell heterostructures.

	optical modulations (%)	coloration times (s)	bleaching times (s)	cathodic charge densities (mC/cm^2)	coloration efficiencies (cm^2/C)	degradation of optical modulation after 1000 cycles (%)
a-WO$_x$ nanorods	45	39	6	9.5	102	13.1
h-WO$_3$/a-WO$_x$ core/shell heterostructures	44	41	6	8.0	82	6.0
h-WO$_3$ nanorods	25	65	6	7.7	43	4.9

tungsten oxide. This makes the material slightly metallic with a small increase in absorption across the spectrum, and a slight increase in reflection in the infrared. Therefore, crystalline tungsten oxide films tend to have a smaller degree of color change compared to their amorphous counterparts.[26] This can explain why a-WO$_x$ nanorods exhibit a much higher optical modulation than h-WO$_3$ nanorods. Similar results have been reported by other researchers.[27-29]

For the case of h-WO$_3$/a-WO$_x$ core/shell heterostructures, the coloration mechanism might be attributed to the combined effect resulted from both small polaron absorption and Drude-like free electron scattering. Fig. 6 schematically illustrates possible working principle of EC device based on h-WO$_3$/a-WO$_x$ core/shell heterostructures. The thicknesses of a-WO$_x$ shells are only about 8 nm, this cannot prevent Li$^+$ ions from penetrating into the underlying crystalline h-WO$_3$ cores. It is then reasonable to expect that the insertion of Li$^+$ ions and electrons into h-WO$_3$/a-WO$_x$ core/shell heterostructures will form small polarons in the a-WO$_x$ shells, and free electrons in crystalline h-WO$_3$ cores. It is also known that the kinetics of ion intercalation can be provided by a diffusion constant, which depends on ionic species, relative film density, intercalation level, temperature, and so on. In general, Li$^+$ ion diffusion in amorphous tungsten oxide is much faster than that in crystalline tungsten oxide, and the diffusion coefficient of Li$^+$ ion will drop rapidly as intercalation level increases.[3] Moreover, it is been reported that the volumetric charge density for a fully tinted WO$_3$ is 68 mC/cm^2·μm,[30] and the extinction coefficient k of tinted WO$_3$ at λ = 550 nm increases from 0 to 0.19 when injected charge density increases from 0 (clear state) to 68 mC/cm^2·μm (fully tinted state).[31] During coloration, the Li$^+$ intercalation level in a-WO$_x$ shells will increase rapidly once a coloration voltage is applied, and shortly develop into the fully tinted state, while the intercalation level in the crystalline h-WO$_3$ cores will gradually increase. After a short time, the volumetric charge density will reach 68 mC/ cm^2·μm in a-WO$_x$ shell and then decrease abruptly with distance from a-WO$_x$/h-WO$_3$ interface, as shown in Fig. 6(b). As a result, incident photons will be absorbed mainly by small polarons in a-WO$_x$ shells and partially by free electrons in crystalline h-WO$_3$ cores, leading to a substantial decrease in transmittance. For bleaching, it is known that the kinetics is governed by a field-driven space-charge limited diffusion current of counter-ions

in M$_x$WO$_3$ next to the electroylte.[4] Since most of the intercalated Li$^+$ ions are accumulated in a-WO$_x$ shells, Li$^+$ deintercalation will occur promptly in h-WO$_3$/a-WO$_x$ core/shell heterostructures once a bleaching voltage is applied, as shown in Fig. 6(d). This leaves a trace amount of Li$^+$ ions in a-WO$_x$ shells and near a-WO$_x$/h-WO$_3$ interfaces.

Apparently, the a-WO$_x$ shells should play a dominant role during coloration and bleaching processes. As our h-WO$_3$/a-WO$_x$ core/shell heterostructures have large specific surface areas, contribution from the a-WO$_x$ shells will be amplified so that the integrated EC device shows similar optical modulation, coloration/bleaching responses, and coloration efficiency to devices based on a-WO$_x$ nanorods. Regarding the durability, it is generally accepted that amorphous tungsten oxides synthesized from wet-chemical methods, suffer from mechanical deterioration and therefore have relatively poor long-term durability. On the other hand, crystalline tungsten oxides with much denser structures have highly improved durability during cycling.[8,18] Recently, Lin et $al.$[32] reported that disordered porous semi-crystalline WO$_3$ films composed of WO$_3$ crystals surrounded by amorphous WO$_3$ layers, demonstrate fast switching kinetics and excellent durability. They suggested that the structural modification (i.e. densification and/or crystallization) occurring in WO$_3$ during extended durability test should be responsible for the improvement in durability. Since the h-WO$_3$/a-WO$_x$ core/ shell heterostructures can be considered to be analogous to their disordered porous semi-crystalline WO$_3$ films, we believe that a similar structural modification is occurring in a-WO$_x$ shells during cyclic stability tests, which is responsible for the good cyclic stability for h-WO$_3$/a-WO$_x$ core/shell heterostructures. Similar enhancements in electrochromic properties have been achieved in electrochromic thin films consisted of monoclinic WO$_x$ nanorods, after post-treated with ozone exposure and thermal annealing.[33] The improvements in optical modulation, coloration efficiency, switching speed, and charge/discharge reversibility are attributed to an ozone induced surface amorphization, meaning that thin amorphous layers form on surfaces of the monoclinic WO$_x$ nanorods after ozone exposure. The resultant tungsten oxide nanostructures are analogous to our h-WO$_3$/a-WO$_x$ core/shell heterostructures.
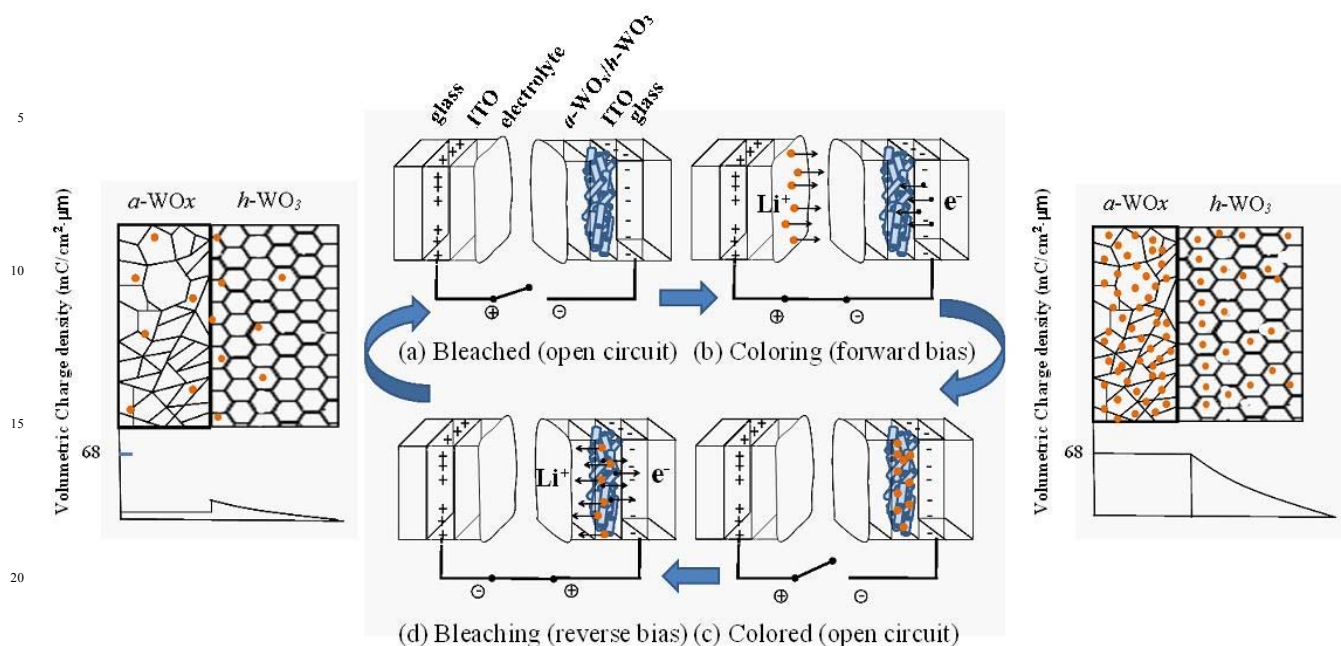
Fig. 6 Schematic illustration of possible working principle for the EC devices based on the *h*-WO₃/*a*-WO$_x$ core/shell heterostructures.

4. Conclusions

One-dimensional *h*-WO₃/*a*-WO$_x$ core/shell heterostructures have been successfully synthesized using a facile two-step hydrothermal method, and the thickness of the *a*-WO$_x$ shell can be controlled by the synthesis time in the second step. The *h*-WO₃/*a*-WO$_x$ core/shell heterostructures combine the assets of the constituent phases, and exhibit highly improved and balanced electrochromic properties. The large optical modulation, fast coloration/bleaching responses, and high coloration efficiency are attributed to the rapid Li$^+$ ion intercalation/deintercalation through the *a*-WO$_x$ shells, and high specific surface areas of the nanoscale core/shell heterostructures. While good cyclic stability may be attributed to the structural modification (i.e. densification and/or crystallization) occurring in the *a*-WO$_x$ shells during cyclic stability tests.

Acknowledgement

Notes and references

^{a}Department of Materials Science and Engineering, National Chung Hsing University, Taichung, Taiwan 40227, R.O.C.
* *E-mail: ycho@dragon.nchu.edu.tw; Fax: (+886)-4 -22857017*
Tel: (+886)-4 -22859112 Ext. 506

1. S. K. Deb, J. A. Chopoorian, *J. Appl. Phys.* 1966, **37**, 4818.
2. S. K. Deb, Appl. *Optics* 1969, **8** S1, 192.
3. C. G. Granqvist, *Sol. Energy Mater. Sol. Cells* 2000, **60**, 201.
4. P. M. S. Monk, *Crit. Rev. Solid State Mater. Sci.* 1999, **24**, 193.
5. M. Deepa, A. G. Joshi, A. K. Srivastava, S. M. Shivaprasad, S. A. Agnihotry, *J. Electrochem. Soc.* 2006, **153**, C365.
6. M. Deepa, T. K. Saxena, D. P. Singh, K. N. Sood, S. A. Agnihotry, *Electrochim. Acta* 2006, **51**, 1974.
7. A. Subrahmanyam, A. Karuppasamy, *Sol. Energy Mater. Sol. Cells* 2007, **91**, 266.
8. S. H. Lee, R. Deshpande, P. A. Parilla, K. M. Jones, B. To, A. H. Mahan, A. G. Dillon, *Adv. Mater.* 2006, **18**, 763.
9. M. Yang, N. K. Shrestha, P. Schmuki, *Electrochem. Commun.* 2009, **11**, 1908.
10. J. Wang, E. Khoo, P. S. Lee, J. Ma, *J. Phys. Chem. C* 2008, **112**, 14306.
11. A. Antonaia, M. L. Addonizio, C. Minarini, T. Polichetti, M. Vittori-Antisari, *Electrochim. Acta* 2001, **46**, 2221.
12. S. Sallard, T. Brezesinski, B. M. Smarsly, *J. Phys. Chem. C* 2007, **111**, 7200.
13. M. Deepa, A. K. Srivastava, K. N. Sood, S. A. Agnihotry, *Nanotechnology* 2006, **17**, 26255.
14. C.-C. Liao, F.-R. Chen, J.-J. Kai, *Sol. Energy Mater. Sol. Cells* 2006, **90**, 1147.
15. Z. Gu, H. Li, T. Zhai, W. Yang, Y. Xia, Y. Ma, J. J. Yao, *Solid State Chem.* 2007, **180**, 98.
16. I. M. Szilágyi, J. Madarász, G. Pokol, P. Király, G. Tárkányi, S. Saukko, J. Mizsei, A. L. Tóth, A. Szabó, K. Varga-Josepovits, *Chem. Mater.* 2008, **20**, 4116.
17. S. Y. Park, J. M. Lee, C. Noh, S. U. Son, *J. Mater. Chem.* 2009, **19**, 7959.

18. K. S. Ahn, Y. C. Nah, Y. E. Sung, K. Y. Cho, S. S. Shin, J. K. Park, *Appl. Phys. Lett.* 2002, **81**, 3930.

19. R. Deshpande, S.-H. Lee, A. H. Mahan, P. A. Parilla, K. M. Jones, A. G. Norman, B. To, J. L. Blackburn, S. Mitra, A. C. Dillon, *Solid State Ionic* 2007, **178**, 895.

20. H. Zheng, J. Z. Ou, M. S. Strano, R. B. Kaner, A. Mitchell, K. Kalantar-zadeh, *Adv. Funct. Mater.* 2011, **21**, 2175.

21. S. H. Lee, H. M. Cheong, C. E. Tracy, A. Mascarenhas, A. W. Czanderna, *Appl. Phys. Lett.* 1999, **75**, 1541.

22. O. F. Schirmer, V. Wittwer, G. Baur, G. Brandt, *J. Electrochem. Soc.* 1977, **124**, 749.

23. C. G. Granqvist, *Sol. Energy Mater. Sol. Cells* 1994, **32**, 369.

24. T. Nanba, M. Ishikawa, Y. Sakai, Y. Miura, *Thin Solid Films* 2003, **445**, 175.

25. D. Dini, F. Decker, E. Masetti, *J. Appl. Electrochem.* 1996, **26**, 647.

26. T. Yoshimura, *J. Appl. Phys.* 1985, **57**, 911.

27. E. Ozkan, S. H. Lee, C. E. Tracy, J. R. Pitts, S. K. Deb, *Sol. Energy Mater. Sol. Cells* 2003, **79**, 439.

28. H. Kamal, A. A. Akl, K. Abdel-Hady, *Physica B* 2004, **349**, 192.

29. A. A. Joraid, *Curr. Appl. Phys.* 2009, **9**, 73.

30. M. Rubin, K. von Rottkay, S.-J. Wen, N. Ozer, J. Slack, *Sol. Energy Mater. Sol. Cells* 1998, **54**, 49.

31. K. von Rottkay, M. Rubin, S.-J. Wen, *Thin Solid Films* 1997, **306**, 10.

32. F. Lin, J. Cheng, C. Engtrakul, A. C. Dillon, D. Nordlund, R. G. Moore, T. C. Weng, S. K. R. Williams, R. M. Richards, *J. Mater. Chem.* 2012, **22**, 16817.

33. F. Lin, C. P. Li, G. Chen, R. C. Tenent, C. A. Wolden, D. T. Gillaspie, A. C. Dillon, R. M. Richards, C. Engtrakul, *Nanotechnology* 2012, **23**, 255601.

CrystEngComm Accepted Manuscript